RESEARCH PAPER

Long-term "memory" of extraordinary climatic seasons in the hysteretic seepage of an unsaturated infinite slope

Diana Bianchi[1] · Domenico Gallipoli[1] · Rossella Bovolenta[1] · Martino Leoni[1,2]

Abstract

This paper presents a study of the hydraulic response of an infinite unsaturated slope exposed to a perturbation of the ordinary seasonal climatic cycle. The ground flow is modelled via a simplified one-dimensional finite difference scheme by decomposing the two-dimensional slope seepage into antisymmetric and symmetric parts. The numerical scheme incorporates two distinct hysteretic and non-hysteretic soil water retention laws, whose parameters have been selected after a preliminary sensitivity analysis. Results indicate that, in the hysteretic case, the "memory" of the perturbation takes a long time to fade, and the ordinary soil saturation cycle is only restored after several years of normal weather. Instead, in the non-hysteretic case, the recovery of the ordinary saturation regime is almost immediate after the perturbation. In contrast with the markedly different predictions of degree of saturation, both hysteretic and non-hysteretic slope models predict virtually identical evolutions of negative pore water pressures, with an almost immediate restoration of the ordinary cycle after the perturbation.

List of symbols

α	Permeability law parameter
β	Slope angle
β_d	Scanning drying shape parameter
β_w	Scanning wetting shape parameter
e	Void ratio
f	Nodal retention flag
γ_w	Water specific weight
γ_{wx^*}	Antisymmetric water specific weight
γ_{wy^*}	Symmetric water specific weight
G_s	Soil specific gravity
h	Piezometric head
h^{asym}	Antisymmetric piezometric head
h^{sym}	Symmetric piezometric head
j	Node number
K	Permeability
κ	Intrinsic permeability
κ_r	Relative permeability
k	Iteration number
K^{sat}	Saturated permeability
K^{asym}	Antisymmetric permeability
K^{sym}	Symmetric permeability
λ_s	Asymptotic slope of main drying/wetting curves
L	Slope thickness
μ	Water dynamic viscosity
m_d	Main drying deviation from asymptote
m_w	Main wetting deviation from asymptote
n	Porosity
(O, x^*, y^*)	Rotated reference system
(O, x, y)	Standard reference system
q^t	Top infiltration rate
$q_{x^*}^{asym}$	Antisymmetric flux parallel to the slope
$q_{y^*}^{asym}$	Antisymmetric flux perpendicular to the slope
$q_{x^*}^{sym}$	Symmetric flux parallel to the slope
$q_{y^*}^{sym}$	Symmetric flux perpendicular to the slope
q_{x^*}	Actual flux parallel to the slope
q_{y^*}	Actual flux perpendicular to the slope
t	Time
S_r	Degree of saturation

✉ Domenico Gallipoli
domenico.gallipoli@unige.it

[1] Dipartimento di Ingegneria Civile, Chimica e Ambientale, Università di Genova, Via Montallegro, 1, 16145 Genoa, Italy

[2] WeSI Geotecnica Srl, Genoa, Italy

s	Suction
$\bar{s}$	Scaled suction
u	Pore water pressure
u_a	Pore air pressure
u^b	Bottom pore water pressure
u^t	Top pore water pressure
u^{asym}	Antisymmetric pore water pressure
u^{sym}	Symmetric pore water pressure
w	Gravimetric water content
ω_d	Intercept of drying asymptote with $S_r = 1$ axis
ω_w	Intercept of wetting asymptote with $S_r = 1$ axis

1 Introduction

The degree of water saturation inside unsaturated soil slopes increases significantly during wet climatic spells especially at shallow depths [15, 19, 38] resulting in a decrease in pore suction. The pore suction is the difference between pore air and water pressures and, in most engineering applications, it coincides with the pore water pressure changed of sign because the pore air pressure is equal to the atmospheric value of zero. A decrease in pore suction inside an unsaturated slope produces a reduction of the cohesive component of strength (i.e. a reduction of the apparent cohesion) and an augmentation of water permeability [1, 4, 28, 32, 33]. This explains the higher frequency of landslides during intense meteoric spells [9, 16, 34, 42] such as, for example, in Alpine regions where slope instabilities present distinct seasonal trends [40] with an increase in failures during late winter and early spring when the ground is wettest.

Some authors have also highlighted the importance of considering the soil hydraulic hysteresis for the accurate calculation of the groundwater regime [2, 8, 30, 43, 44], though most models still adopt non-hysteretic (i.e. reversible) water retention laws to simplify the analysis. The few published investigations of hysteretic seepage refer to horizontal ground [3, 14, 41, 45], with only a handful of studies about sloping ground [24, 31].

The present paper analyses the hysteretic hydraulic response of an infinite unsaturated slope to seasonal climatic cycles by combining the seepage decomposition method of Bianchi et al. [5, 6] with the hysteretic retention law of Gallipoli et al. [21]. Bianchi et al. [5] demonstrated that the two-dimensional seepage across an infinite slope can be solved by using the one-dimensional Richards'

equation for horizontal ground, provided that the soil permeability and water specific weight are both scaled by the cosine of the slope angle. Gallipoli et al. [21] formulated a hysteretic retention law accounting for irreversible changes of degree of saturation during cycles of both suction and void ratio. The hysteretic retention law of Gallipoli et al. [21] is chosen because it consists of two closed form expressions for drying and wetting paths, respectively, which can be directly implemented into computational routines without the need of numerical integration, thus increasing accuracy of predictions. Nevertheless, the proposed algorithm is general and can be adapted, with relative ease, to accommodate other types of hysteretic retention models [e.g. 26, 36].

In this paper, a detailed sensitivity analysis of the adopted retention law is first presented to define a set of model parameter values allowing a realistic exploration of the effect of hydraulic hysteresis on ground behaviour. The retention law is then implemented within a one-dimensional finite difference scheme [7, 13, 18, 29, 35, 39], which exploits the above decomposition methodology to calculate the seepage regime inside an unsaturated infinite slope exposed to seasonal variations of pore suction at the ground surface. The finite difference scheme is finally used to analyse the response of the slope to two extraordinary dry and wet spells perturbing the "equilibrium" seepage cycle, which is attained after a prolonged sequence of ordinary climatic seasons. Due to the hysteretic nature of the soil, the "memory" of this perturbation takes a long time to fade, and the equilibrium seepage cycle is only restored after several years of ordinary weather. Conversely, in the case of non-hysteretic seepage, the recovery of the ordinary seepage regime is almost immediate after the perturbation has ended.

The above results highlight the importance of incorporating hydraulic hysteresis for the accurate prediction of pore water pressure and degree of saturation in slopes exposed to varying climatic conditions and, hence, for the development of robust landslide early-warning systems. Yet, the conclusions of this work should be treated as preliminary and need corroboration by future studies using alternative constitutive laws to model groundwater hysteresis.

2 Hysteretic soil water retention model

The main aspects of the hysteretic retention law of Gallipoli et al. [21] are here briefly recalled with a specific focus on the equations used in the following part of the paper. This retention law relates the degree of saturation S_r to a scaled suction variable $\bar{s}$ via an approach that is coherent with the tenets of bounding surface plasticity. To

Table 1 Reference parameter ranges and base values for main drying and wetting curves

Parameters	Reference range	Base value
λ_s (–)	0.1–1	1
ω_w (kPa)	50–500	50
ω_d (kPa)	100–1000	1000
m_d (–)	0.1–1	0.1
m_w (–)	0.1–1	1

incorporate the dependency of degree of saturation on both suction s and void ratio e, the scaled suction $\bar{s}$ is defined as:

$$\bar{s} = se^{\frac{1}{\lambda_s}} \tag{1}$$

where λ_s is a model parameter. For simplicity, in this work, the soil is assumed rigid and the void ratio is fixed at one, which implies that the scaled suction $\bar{s}$ of Eq. (1) coincides with the suction s (it also means that the degree of saturation S_r coincides with the product of the gravimetric water content w and the constant specific gravity G_s, i.e. $S_r = wG_s$).

Based on this assumption, the model of Gallipoli et al. [21] postulates the existence of two bounding curves, i.e. a main drying and a main wetting curve, which delimit the region of admissible soil states in the $S_r - s$ plane. Both main curves have the following mathematical form:

$$S_r = \left[1 + \left(\frac{s}{\omega_i}\right)^{\lambda_s/m_i}\right]^{-m_i} \tag{2}$$

where the subscript 'i' coincides with 'd' or 'w' depending on whether Eq. (2) refers to a main drying or wetting curve. Therefore, in addition to λ_s, four extra parameters are required to define the main hysteretic loop, namely two parameters for the main drying curve, i.e. ω_d and m_d, and two parameters for the main wetting curve, i.e. ω_w and m_w.

Inside this admissible region, the retention behaviour is described by two families of scanning drying and wetting curves, which tend asymptotically to the respective main curves. This asymptotic scanning behaviour is modelled by assuming a specific mathematical expression for the drying and wetting derivatives, which are then integrated in a closed form into the following two equations:
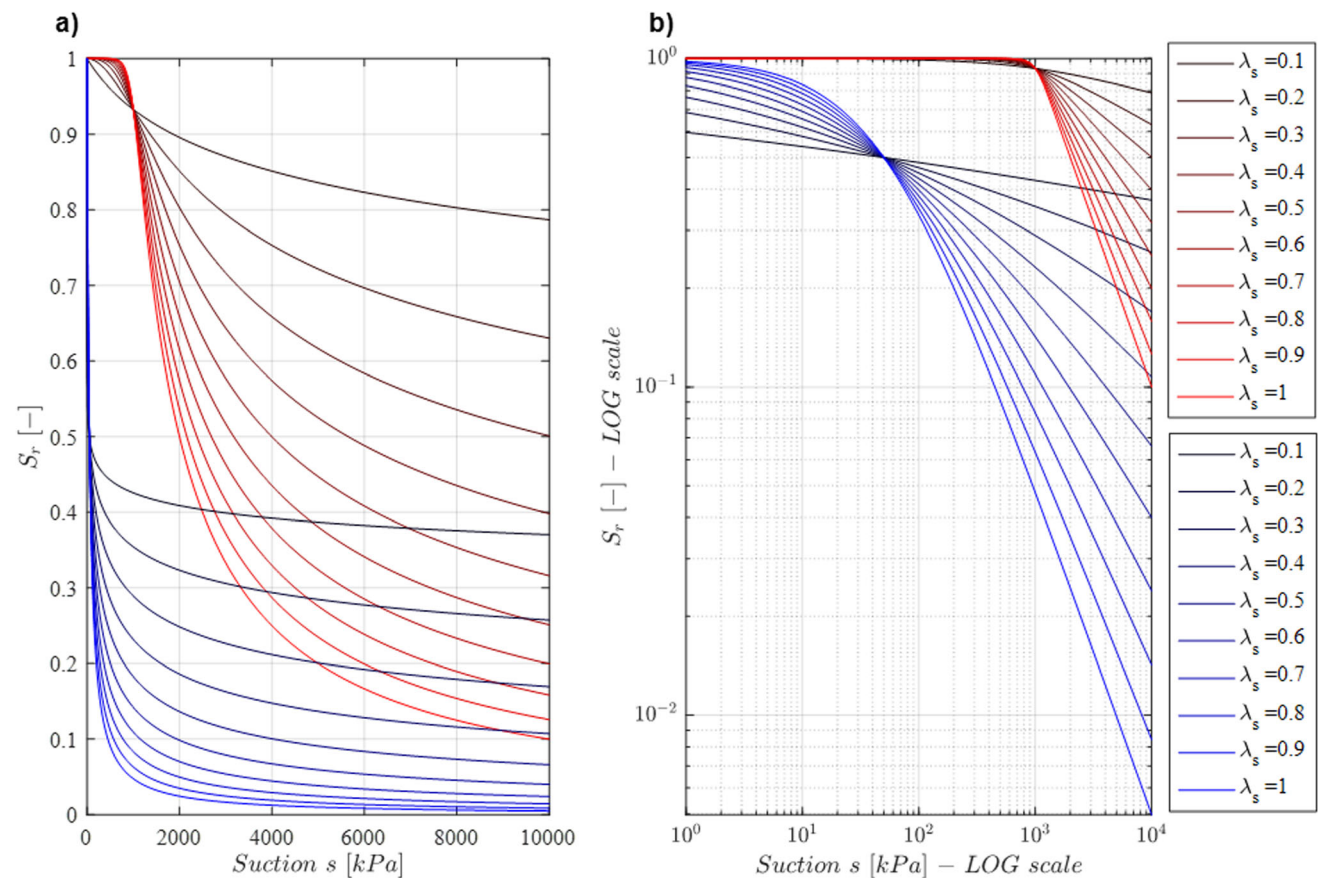
Fig. 1 Influence of parameter λ_s on main drying curves (red) and main wetting curves (blue): **a** natural scale and **b** logarithmic scale (color figure online)
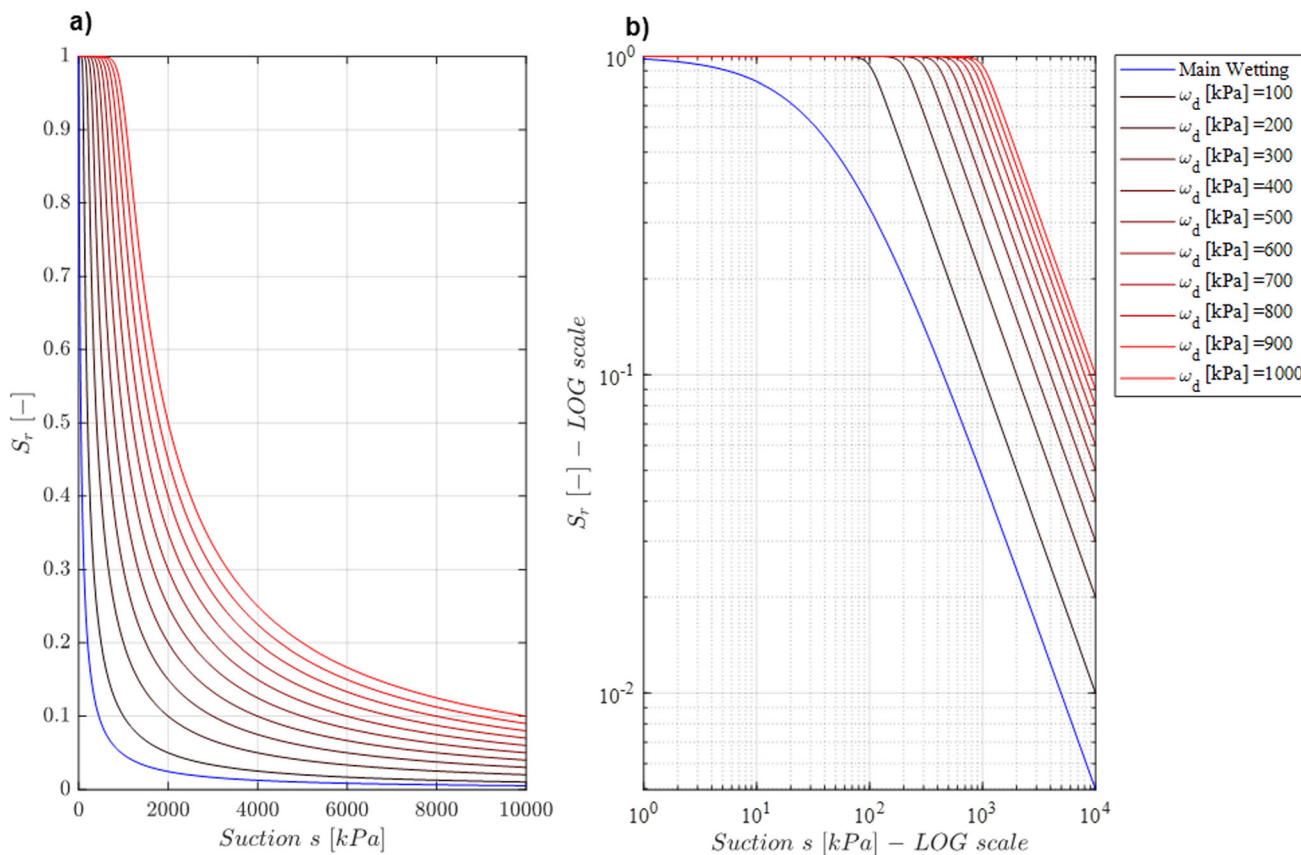
Fig. 2 Influence of parameter ω_d on main drying curves (red): **a** natural scale and **b** logarithmic scale (in blue the main wetting curve corresponding to the base value of ω_w) (color figure online)

$$S_{rd} = \left[1 + \left(\frac{s^{\beta_d} + C_d}{\omega_d^{\beta_d}}\right)^{\lambda_s/(\beta_d m_d)}\right]^{-m_d} \quad (3)$$

$$S_{rw} = \left[1 + \left(\frac{s^{\beta_w}}{\omega_w^{\beta_w}(1 + C_w s^{\beta_w})}\right)^{\lambda_s/(\beta_w m_w)}\right]^{-m_w} \quad (4)$$

where β_d and β_w are two additional parameters defining the shape of the scanning drying and wetting curves while C_d and C_w are the two non-negative constants of integration. Note that, if the two constants of integration are zero, Eqs. (3) and (4) reduce to the respective main curves.

Within the two families of scanning curves defined by Eqs. (3) and (4), each individual curve is identified by a different value of the constant of integration, which is calculated by imposing a boundary condition. For example, if the initial soil state lies on a drying path (i.e. a path with increasing suction), Eq. (3) is used and the constant of integration C_d is evaluated by imposing the passage of the curve through a point of known coordinates (S_{r0}, s_0) as:

$$C_d = \omega_d^{\beta_d}\left(S_{r_0}^{-1/m_d} - 1\right)^{\beta_d m_d/\lambda_s} - s_0^{\beta_d} \quad (5)$$

If the soil subsequently switches to a wetting path (i.e. a path with decreasing suction), Eq. (4) is employed and the constant of integration C_w is evaluated by imposing the passage of the curve through the reversal point (the point marking the end of previous drying and the start of the subsequent wetting) of coordinates $(S_{r\text{rev}}, s_{\text{rev}})$ as:

$$C_w = \frac{1}{\omega_w^{\beta_w}}\left(S_{r_{\text{rev}}}^{-1/m_w} - 1\right)^{-\beta_w m_w/\lambda_s} - \frac{1}{s_{\text{rev}}^{\beta_w}} \quad (6)$$

Further details about this hysteretic law and the corresponding parameter calibration are found in [20-22]

3 Parametric analysis of hysteretic soil water retention law

This section explores the effect of each parameter in the hysteretic retention law of Gallipoli et al. [21] on the predicted soil response. First, the five parameters
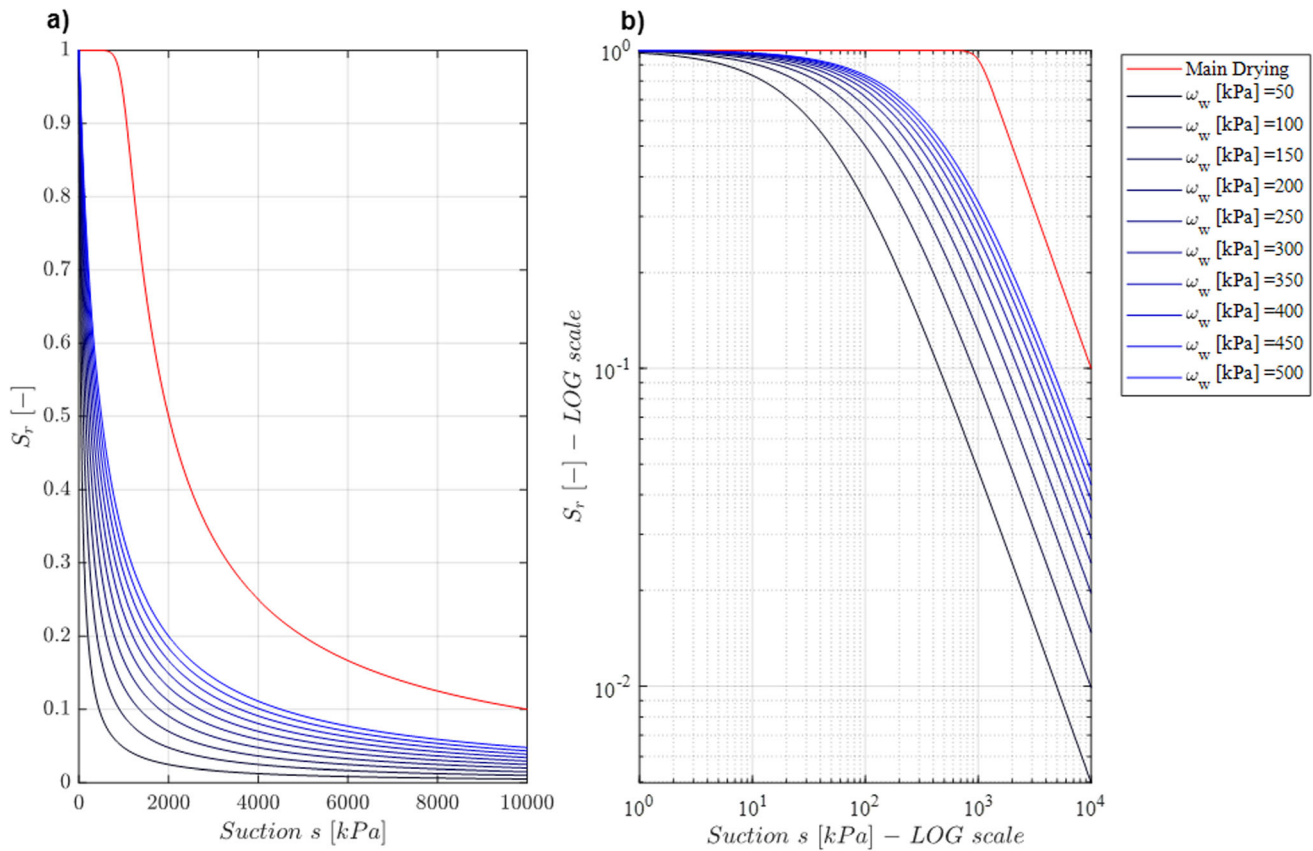
Fig. 3 Influence of parameter ω_w on main wetting curves (blue): **a** natural scale and **b** logarithmic scale (in red the main drying curve corresponding to the base value of ω_d) (color figure online)

$\lambda_s, \omega_w, \omega_d, m_d$ and m_w defining the two main curves, and hence the region of admissible soil states in the $S_r - s$ plane, are considered. As shown in Gallipoli et al. [21], these parameters must satisfy the following restrictions to ensure realistic predictions of the two main curves:

$$\begin{cases} \lambda_s > 0 \\ \omega_d \geq \omega_w > 0 \\ m_w \geq m_d > 0 \end{cases} \tag{7}$$

Table 1 presents the reference parameter ranges according to published data for clay and silty soils [11, 21], together with the corresponding base values used in the following sensitivity analysis.

Figure 1 shows the predicted main drying and wetting curves corresponding to distinct values of λ_s in the reference range while the remaining parameters are fixed at their base values (Table 1). The parameter λ_s coincides with the slope of the linear asymptotes of the main drying and wetting curves in the $\log S_r - \log s$ plane (Fig. 1b). Inspection of Fig. 1 indicates that larger values of λ_s correspond to steeper curves and, hence, an increasingly sub-vertical admissible region enforcing greater changes of degree saturation over smaller suction intervals.

Figures 2 and 3 show the predicted main drying and wetting curves corresponding to distinct values of ω_d and ω_w in their respective reference ranges while the remaining parameters are fixed at their base values (Table 1). The parameters ω_d and ω_w represent the intercepts of the linear asymptotes of the corresponding main curve with the horizontal axis at full saturation in the $\log S_r - \log s$ plane (Figs. 2b and 3b). These two parameters are therefore directly related to the air entry and expulsion values of the soil, which explains why ω_d cannot be smaller than ω_w according to Eq. (7). Inspection of Figs. 2 and 3 indicates that larger values of ω_d and ω_w cause a shift of the corresponding main curve towards the higher suction range, while larger differences between these two values result in a wider admissible region.

Figure 4 shows the predicted main drying and wetting curves corresponding to distinct values of m_d and m_w in their respective reference ranges while the remaining parameters are fixed at their base values (Table 1). Inspection of Fig. 4a indicates that bigger differences between m_d and m_w result in a larger horizontal distance between the two main curves in the $S_r - s$ plane. Similarly, inspection of Fig. 4b indicates that greater values of m_d and m_w produce a larger deviation of the main curves from their
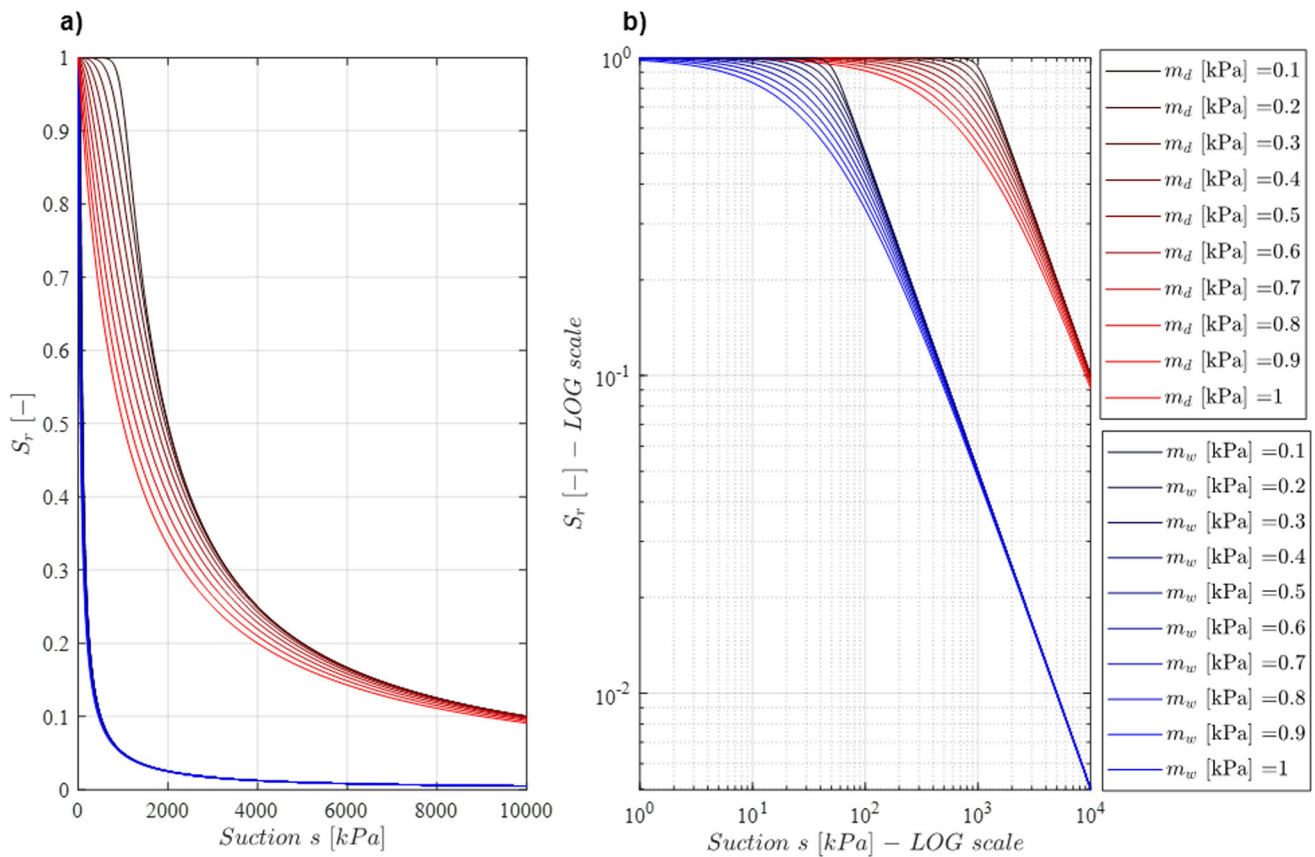
Fig. 4 Influence of parameters m_d and m_w on the main drying curves (red) and main wetting curves (blue): **a** natural scale and **b** logarithmic scale (color figure online)

Table 2 Reference parameter ranges for scanning drying and wetting curves

Parameters	Reference range
β_d (–)	1.5–3.5
β_w (–)	0.5–2.5

respective linear asymptotes in the $\log S_r - \log s$ plane. The values of m_d and m_w must be both positive, as prescribed by Eq. (7), to ensure that the predicted degree of saturation is bounded between zero and one. Moreover, m_w cannot be smaller than m_d to prevent that the two curves cross each other close to full saturation.

Next, the behaviour inside the admissible region is explored by varying the parameters β_d and β_w, which govern the shape of the scanning drying and wetting curves, respectively. As demonstrated by Gallipoli et al. [21] (see also corrigendum to this reference), the values of β_d and β_w must comply with the following two restrictions to ensure the prediction of realistic scanning curves:

$$\begin{cases} \beta_d > 1 \\ \beta_w > 0 \end{cases} \tag{8}$$

In the following, the values of β_d and β_w are varied inside their respective reference ranges of Table 2 while the parameters of the two main curves are fixed at their base values of Table 1.

Figure 5 shows three groups of scanning drying curves and three groups of scanning wetting curves inside the admissible region, with each group starting from the same soil state. The different curves of each group correspond to varying values of either β_d or β_w depending on whether a scanning drying or wetting curve is considered. Inspection of Fig. 5 indicates that scanning paths become increasingly flatter as the values of β_d or β_w grow large and the initial state is farther away from the respective target main curve. As expected, all scanning paths tend asymptotically towards their respective target main curve when suction increases or decreases.

The model of Gallipoli et al. [21] predicts that an unsaturated soil subjected to repeated suction cycles over a fixed interval will progressively tend towards a "steady
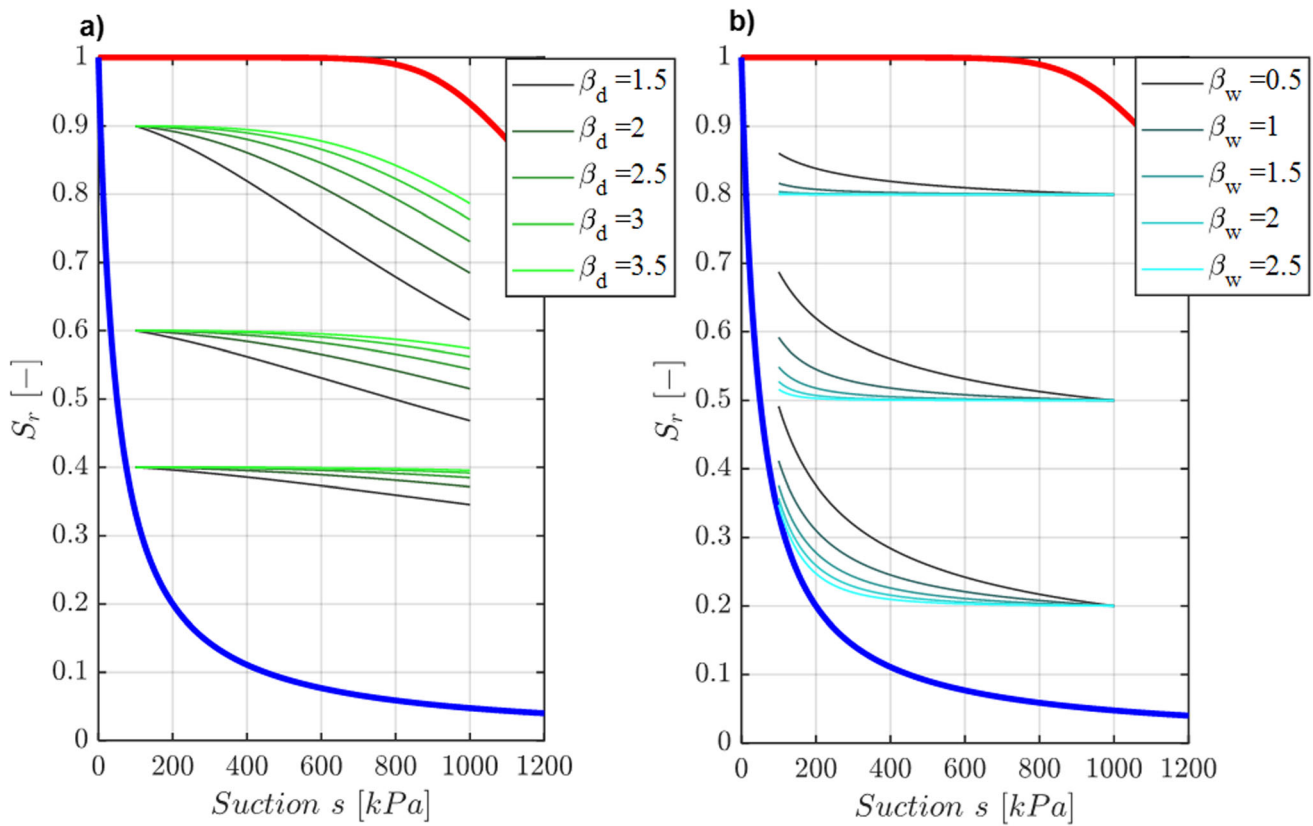
Fig. 5 Influence of parameters β_d and β_w on the **a** scanning drying curves and **b** scanning wetting curves (main drying curve in red and main wetting curve in blue) (color figure online)

Table 3 Combinations of parameters β_d and β_w

| Case 1	Case 2	Case 3	Case 4
$\beta_d = 3.5$	$\beta_d = 1.5$	$\beta_d = 1.5$	$\beta_d = 3.5$
$\beta_w = 0.5$	$\beta_w = 2.5$	$\beta_w = 0.5$	$\beta_w = 2.5$

hysteretic loop" defined by a pair of scanning drying and wetting curves inside the admissible $S_r - s$ region. The steady hysteretic loop is independent of the starting soil state and is only governed by the chosen suction interval, though the initial values of saturation and suction will influence the number of cycles that are necessary to attain the steady hysteretic loop.

The following section explores the effect of different combinations of parameters β_d and β_w on the response of a soil element subjected to repeated suction cycles between 100 and 1000 kPa. This interval has been chosen because it may represent the condition of a slope surface during a sequence of ordinary wet and dry seasons (i.e. the ordinary suction cycle) in a relatively arid climate. Four distinct

combinations of β_d and β_w (Table 3) are analysed and the respective steady hysteretic loops are shown in Fig. 6. The two reversal points of each loop may be interpreted as the state of the slope surface at the end of summer/start of winter and end of winter/start of summer, respectively, during ordinary suction cycles.

In Table 3, case 1 corresponds to the largest value of β_d and the smallest value of β_w in their respective reference ranges, while case 2 corresponds to the smallest value of β_d and the largest value of β_w. Case 3 corresponds instead to the smallest values of both β_d and β_w while case 4 corresponds to the largest values of both β_d and β_w. Inspection of Fig. 6 indicates that the chosen combination of β_d and β_w has a strong influence on the position and amplitude of the steady hysteretic loop inside the admissible region.

A perturbation of the steady hysteretic loop is next produced by an extraordinary decrease or increase in suction which may, for example, occur at the slope surface during an extremely wet or dry season. Here, the wetting perturbation is modelled by a reduction of suction down to 0 kPa, bringing the soil to full saturation, while the drying perturbation is modelled by an increase in suction up to 2000 kPa. In both cases, the perturbation is followed by a
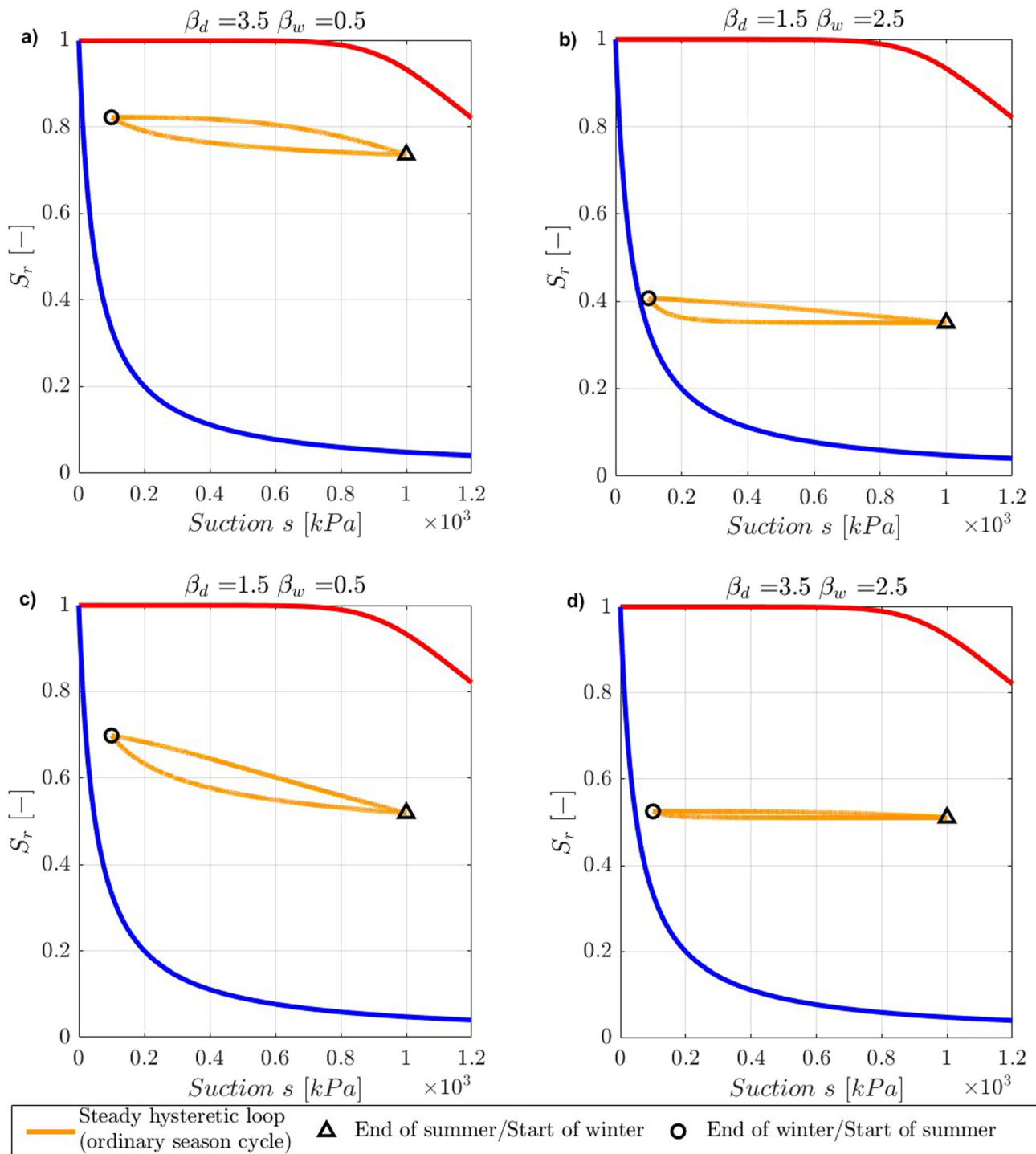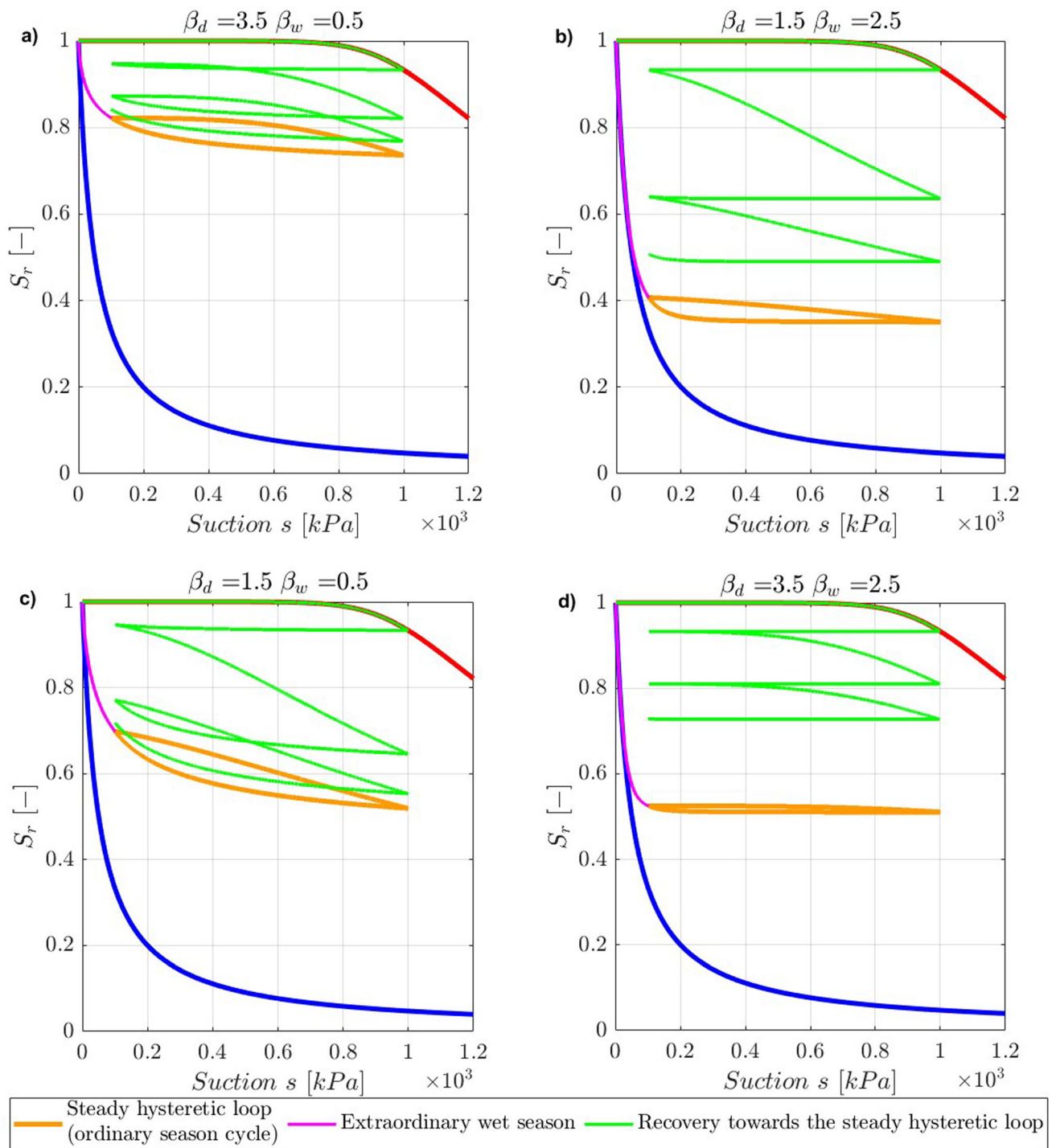
Fig. 6 Influence of different combinations of parameters β_d and β_w on the steady hysteretic loop: **a** case 1, **b** case 2, **c** case 3 and **d** case 4 (main drying curve in red and main wetting curve in blue) (color figure online)
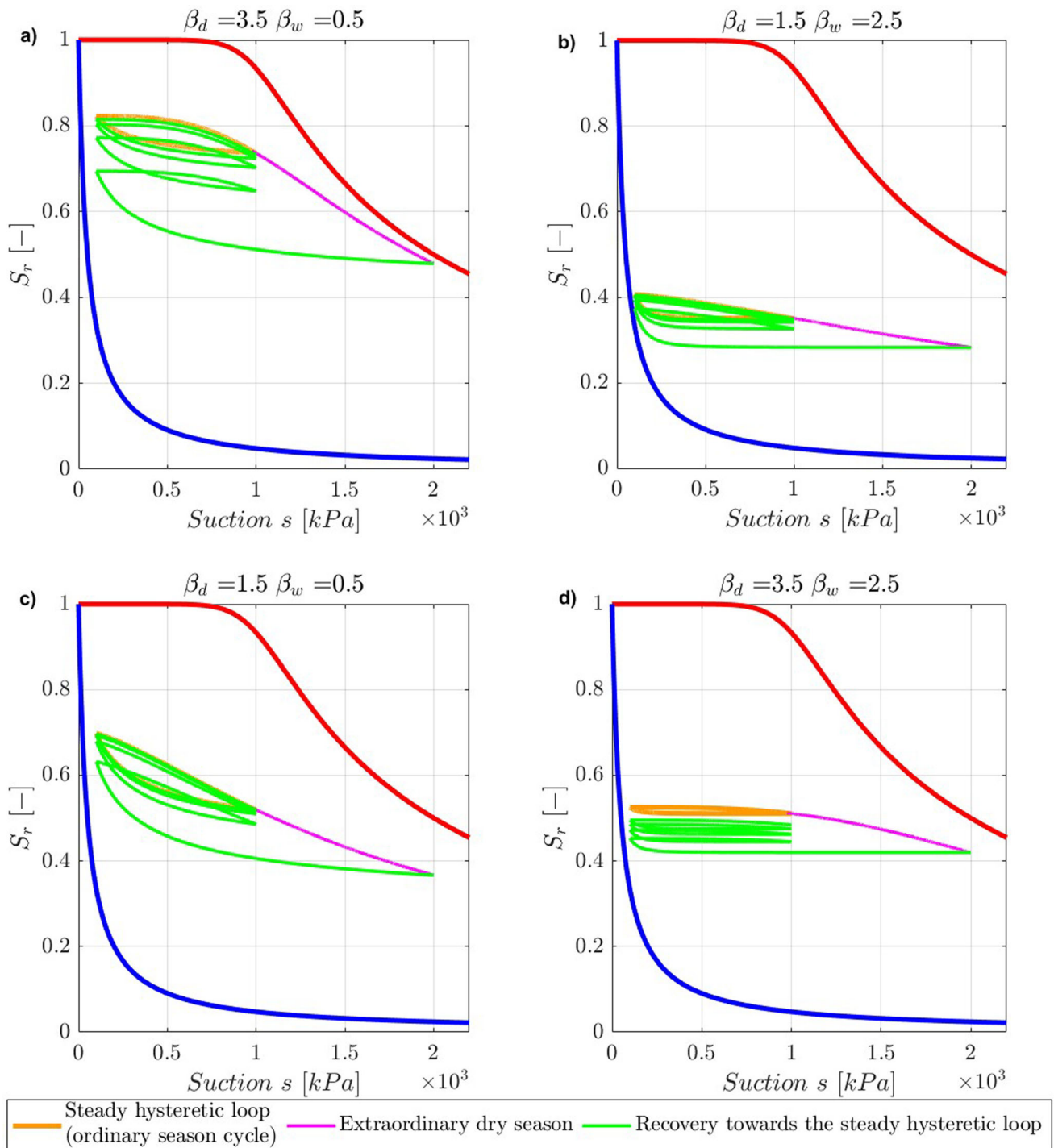
sequence of three ordinary suction cycles between 100 and 1000 kPa pushing the soil gradually back towards the steady hysteretic loop. Figures 7 and 8 show the corresponding predictions for the four different combinations of

β_d and β_w in Table 3, which demonstrate a strong influence of both parameters on the number of ordinary cycles necessary to regain equilibrium. Inspection of Figs. 7 and 8 indicates that a sequence of three ordinary cycles after the

Fig. 7 Influence of different combinations of parameters β_d and β_w on the recovery of steady conditions after a wetting perturbation of the ordinary suction cycle: **a** case 1, **b** case 2, **c** case 3 and **d** case 4 (main drying curve in red and main wetting curve in blue) (color figure online)

Fig. 8 Influence of different combinations of parameters β_d and β_w on the recovery of steady conditions after a drying perturbation of the ordinary suction cycle: **a** case 1, **b** case 2, **c** case 3 and **d** case 4 (main drying curve in red and main wetting curve in blue) (color figure online)
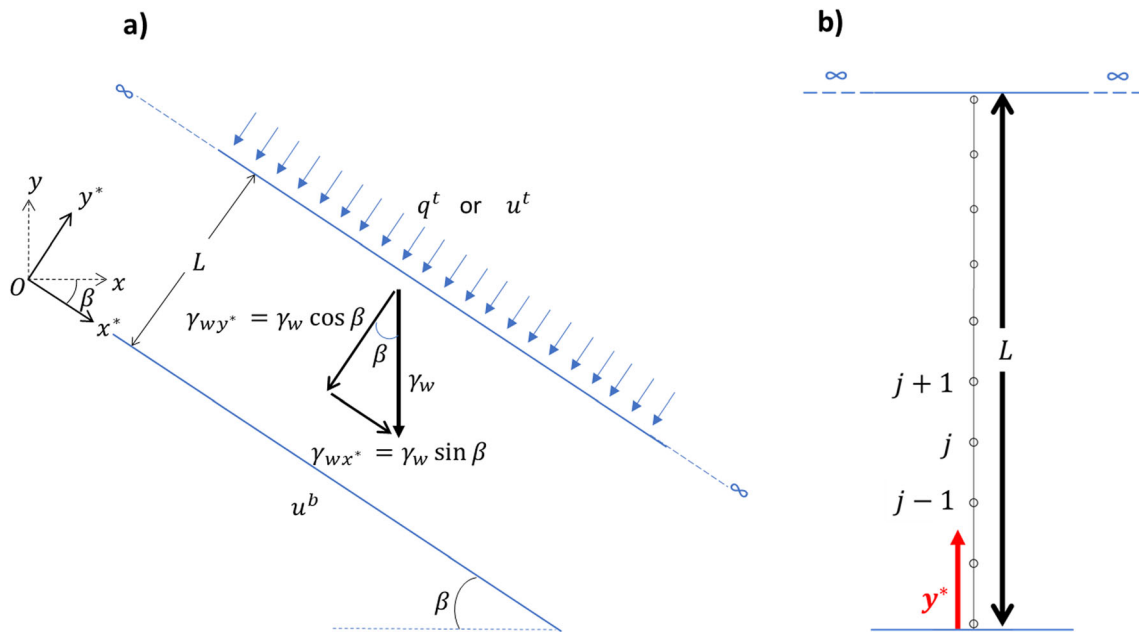
Fig. 9 Model of hysteretic seepage across an infinite unsaturated slope: **a** flow decomposition (Bianchi et al. [5]) and **b** discretised slope section

perturbation is not enough to regain steady conditions, especially for case 4 which exhibits a narrow steady hysteretic loop. To further explore this behaviour in field conditions, the next section studies the response of an infinite slope, at different ground depths, to a perturbation of the ordinary suction cycle at the surface.

4 Model of hysteretic seepage across an infinite unsaturated slope

Bianchi et al. [5] have demonstrated that the two-dimensional seepage across an infinite unsaturated slope (Fig. 9a) can be treated as a one-dimensional infiltration problem by factoring the soil permeability and the water specific weight with the cosine of the slope angle (see Appendix). In this work, the slope seepage is therefore calculated via the following "scaled" version of the one-dimensional Richards' water balance [37], which incorporates the factored soil permeability $K\cos\beta$ and water specific weight $\gamma_w\cos\beta$:

$$n\frac{\partial S_r}{\partial t} = \frac{\partial}{\partial y^*}\left[K\cos\beta\left(1 + \frac{1}{\gamma_w\cos\beta}\frac{\partial u}{\partial y^*}\right)\right] \quad (9)$$

where y^* is the coordinate perpendicular to the slope (Fig. 9a), t is the time, $n = \frac{e}{1+e}$ is the soil porosity (here assumed constant) and u is the pore water pressure, which in unsaturated soils is tensile and therefore negative. The present work assumes that the pore air pressure is constant and fixed to the atmospheric value of zero, which implies that the pore water pressure coincides with the suction changed of sign, i.e. $u = -s$.

In Eq. (9), the unsaturated permeability $K = \kappa_r K^{sat}$ is the product of the constant saturated permeability K^{sat} and the relative unsaturated permeability function κ_r ranging between zero (in fully dry conditions) and one (in fully saturated conditions). The relative unsaturated permeability function is here assumed to coincide with the following exponential function of the negative pore water pressure u:

$$\kappa_r = e^{\alpha u} \quad (10)$$

where α is a soil parameter. The choice of Eq. (10) is consistent with previous infiltration models [23, 25, 27, 46], though alternative forms (e.g. incorporating a dependency on degree of saturation instead of pore water pressure) are also possible. The effect of the specific form of the relative unsaturated permeability function on the predicted slope response is outside the scope of the present investigation and constitutes matter for future research.

Given that $s = -u$, the storage term on the left-hand side of Eq. (9) can be expanded as:

$$n\frac{\partial S_r}{\partial t} = n\frac{\partial S_r}{\partial s}\frac{\partial s}{\partial u}\frac{\partial u}{\partial t} = -n\frac{\partial S_r}{\partial s}\frac{\partial u}{\partial t} \quad (11)$$

where the derivative $\frac{\partial S_r}{\partial s}$ is evaluated from Eqs. (3) or (4) depending on whether the soil is moving along a drying or
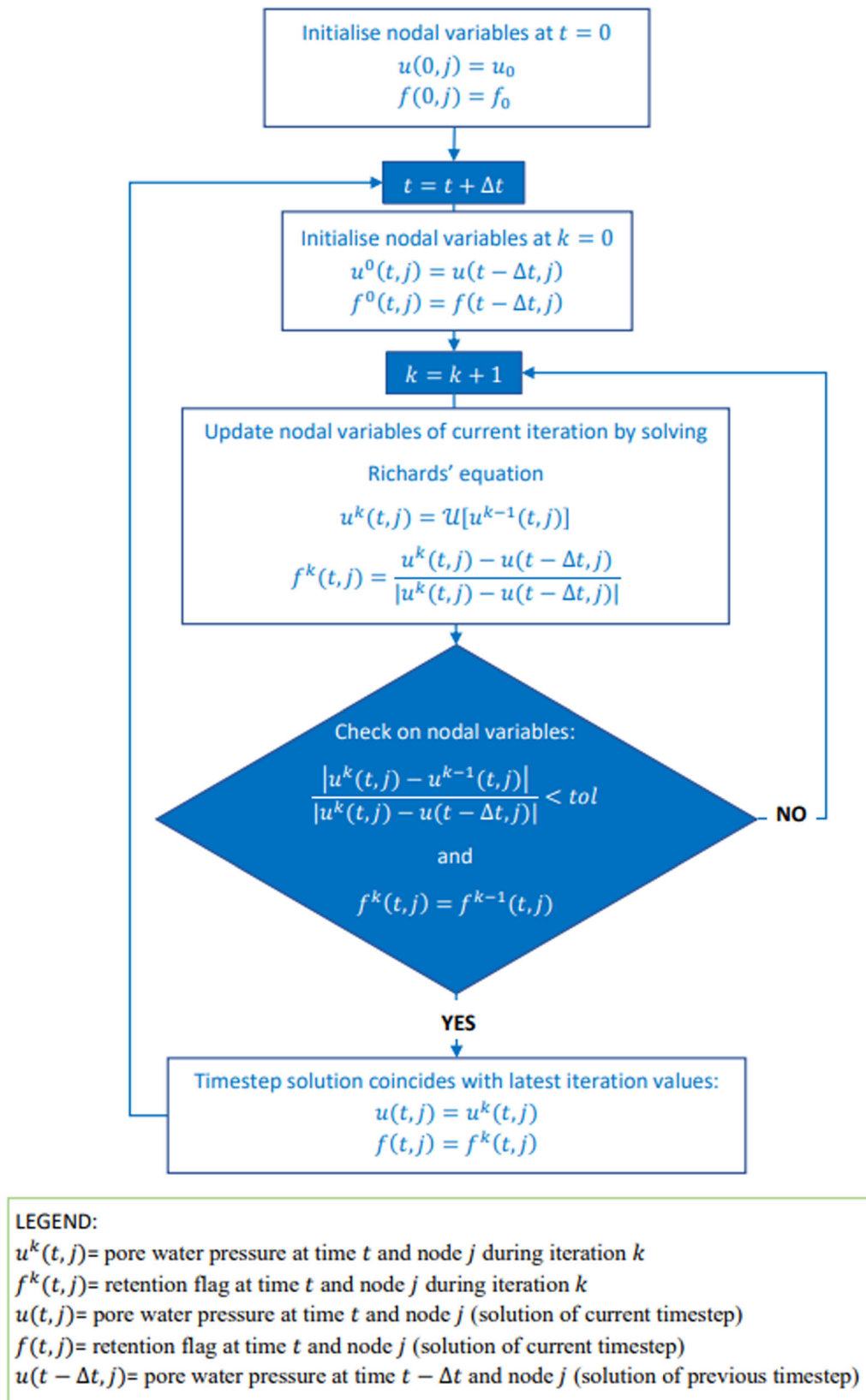
Fig. 10 Implementation of the hysteretic retention law of Gallipoli et al. [21] inside Richards' water balance equation: algorithm flow chart

wetting path. The combination of Eqs. (9), (10) and (11) yields the following non-liner differential equation of the pore water pressure u:

$$-n\frac{\partial S_r}{\partial s}\frac{\partial u}{\partial t} = K^{\text{sat}}\cos\beta\frac{\partial}{\partial y^*}\left[e^{\alpha u}\left(1 + \frac{1}{\gamma_{\text{w}}\cos\beta}\frac{\partial u}{\partial y^*}\right)\right] \quad (12)$$

which is here solved via a one-dimensional finite difference scheme with implicit time discretisation [13, 17, 35, 39]. The scheme is applied to a perpendicular section of the infinite slope of Fig. 9a having thickness L, which is discretized by M equally spaced nodes, as shown in Fig. 9b.

The hysteretic law of Gallipoli et al. [21] is implemented by introducing a nodal retention flag f, which is either -1 or 1 depending on whether the negative pore water pressure u at the node is decreasing (drying) or increasing (wetting). The retention behaviour is therefore calculated by Eq. (3), if $f = -1$, or Eq. (4), if $f = 1$, while the corresponding constant of integration is evaluated by either Eqs. (5) or (6).

Figure 10 shows the flow chart of the proposed iterative algorithm where $u^k(t,j)$ and $f^k(t,j)$ are the pore water pressure and retention flag, respectively, at node j during the iteration k of the current time t. The algorithm begins by fixing the time boundary condition (i.e. at $t = 0$) at each node for both pore water pressure $u(0,j) = u_0$ and retention flag $f(0,j) = f_0$. The time is then incremented to $t = 0 + \Delta t$ and the nodal variables of iteration $k = 0$ are initialised to the values at the end of the previous timestep, i.e. $u^0(t,j) = u(t - \Delta t, j)$ and $f^0(t,j) = f(t - \Delta t, j)$. In each iteration k of time t, the nodal pore water pressures $u^k(t,j)$ are calculated by solving the algebraic system of the discretised Richards' equation, whose nonlinear coefficients are a function of the pore water pressures of the previous iteration $k - 1$, i.e. $u^k(t,j) = \mathcal{U}[u^{k-1}(t,j)]$. The retention flag $f^k(t,j)$ is also updated in each iteration k to either -1 (drying) or 1 (wetting) depending on whether the corresponding pore water pressure $u^k(t,j)$ is smaller or greater than the value at the end of the previous timestep $u(t - \Delta t, j)$. This iterative procedure continues until the following two conditions are simultaneously satisfied at each node: (a) the difference between the pore water pressures calculated in the last two iterations, relative to the increment of the current timestep, is smaller than a given tolerance tol, i.e. $\frac{|u^k(t,j) - u^{k-1}(t,j)|}{|u^k(t,j) - u(t-\Delta t, j)|} < tol$ and (b) the retention flag remains unchanged during the last two iterations, i.e. $f^k(t,j) = f^{k-1}(t,j)$. The latter condition must be satisfied because the pore water pressure at a given node may switch between drying and wetting paths as the algorithm iteratively converges towards the solution of the current time.
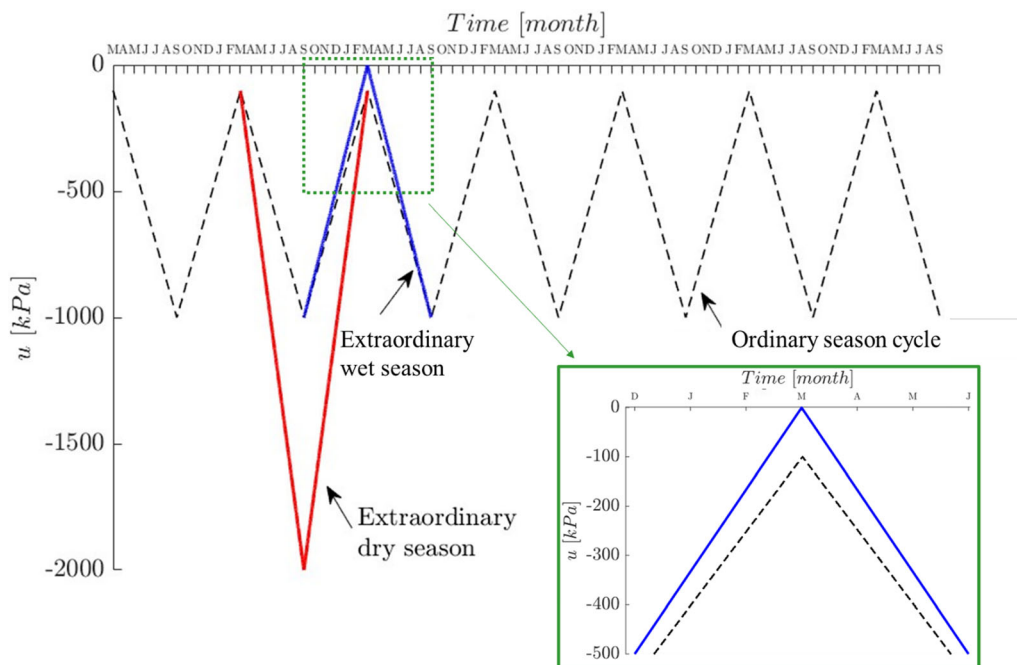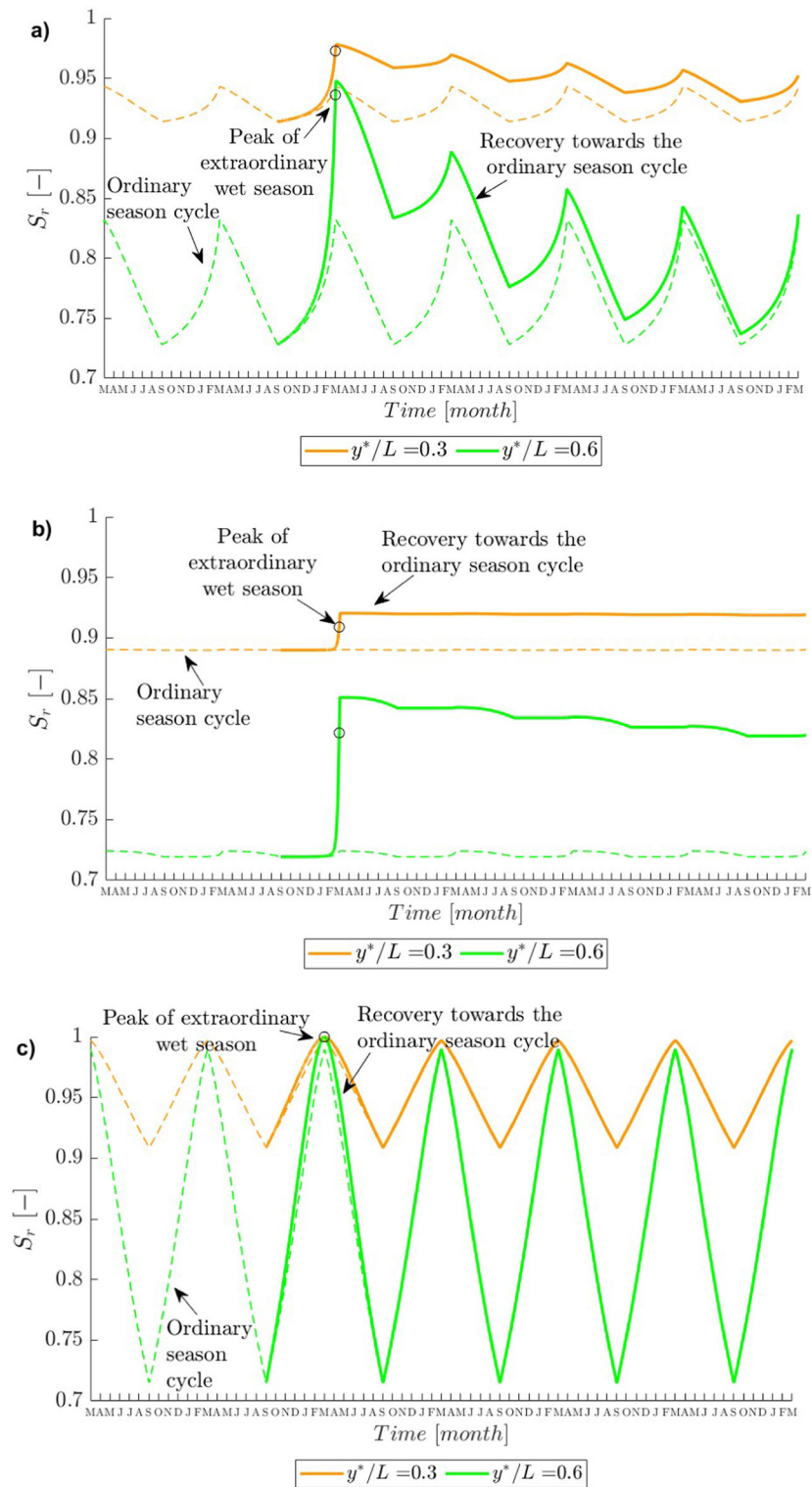

Fig. 11 Pore water pressure cycles at the slope surface (ordinary season cycle in black, extraordinary wet season in blue and extraordinary dry season in red) (color figure online)

Fig. 12 Effect of the extraordinary wet season on the evolution of degree of saturation at the two section coordinates $y^*/L = 0.3$ and $y^*/L = 0.6$: **a** hysteretic model of case 3, **b** hysteretic model of case 4 and **c** non-hysteretic model
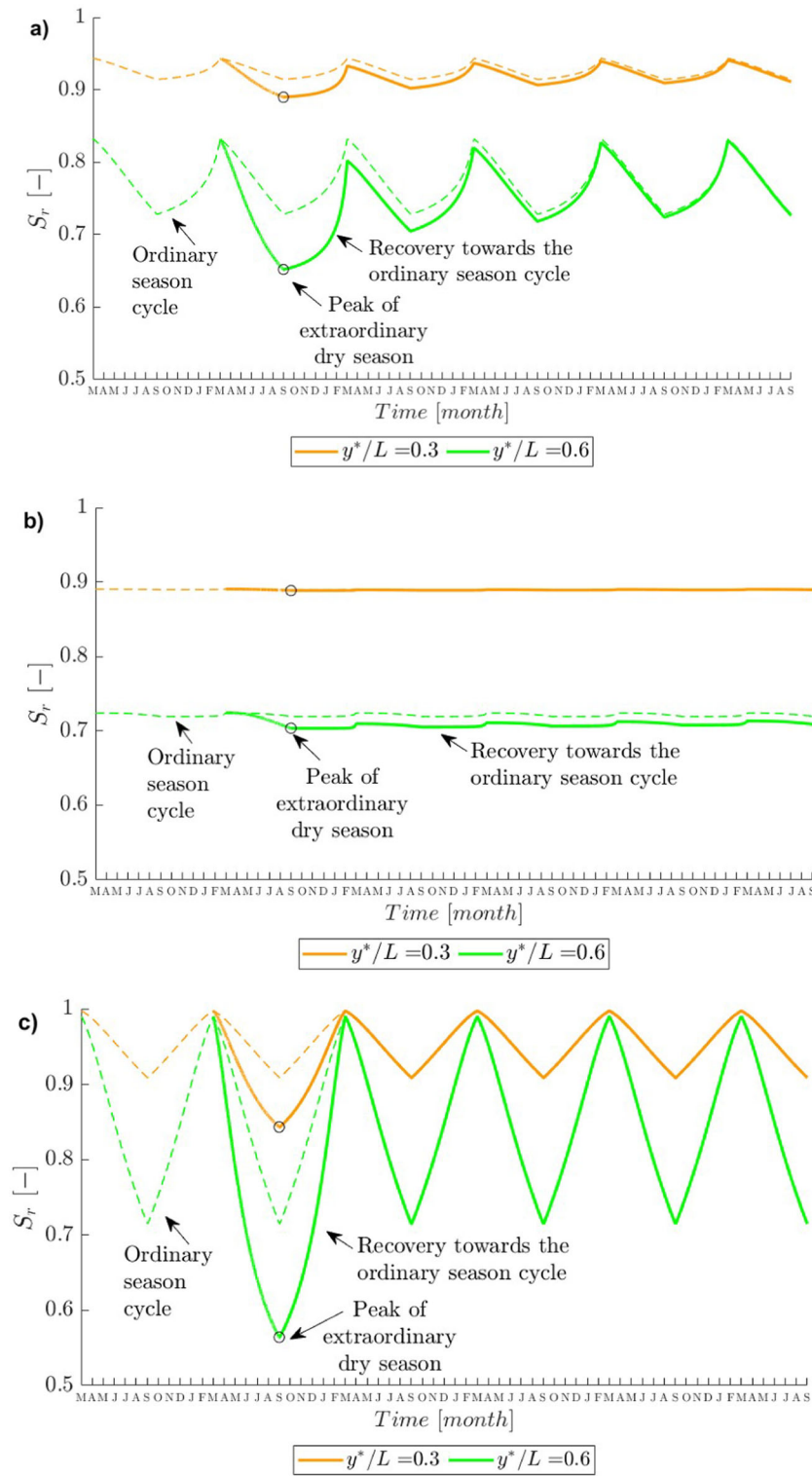
Fig. 13 Effect of the extraordinary dry season on the evolution of degree of saturation at the two section coordinates $y^*/L = 0.3$ and $y^*/L = 0.6$: a hysteretic model of case 3, b hysteretic model of case 4 and c non-hysteretic model

5 Slope memory of extraordinary climatic seasons

The above algorithm is next applied to the simulation of seepage across an infinite slope subjected to a cyclic variation of pore water pressure at the ground surface. The slope has inclination $\beta = 30°$ and is modelled by a one-dimensional mesh of 100 equally spaced nodes (Fig. 9b) representing a section perpendicular to the ground (i.e. a section parallel to the y^* axis of Fig. 9a). Results are presented in terms of the non-dimensional coordinate y^*/L, which allows a normalisation of the seepage profiles for different slope thicknesses L. The saturated permeability is fixed at $K^{\text{sat}} = 10^{-8}$ m/s, while a value of $\alpha = 10^{-3}$ kPa^{-1} is introduced in the relative unsaturated permeability function κ_r of Eq. (10). The groundwater table is fixed at the base of the slope by imposing a constant zero pore water pressure u^b at the bottom boundary (i.e. at $\frac{y^*}{L} = 0$), while the top boundary corresponding to the ground surface (i.e. at $\frac{y^*}{L} = 1$) is subjected to seasonal cycles of pore water pressure u^t.

Figure 11 shows the ordinary seasonal cycle of pore water pressure imposed at the ground surface, which varies linearly between -100 kPa in March and -1000 kPa in September, together with two perturbations corresponding to an extraordinary wet season and an extraordinary dry season. The extraordinary wet season produces a linear increase in pore water pressure from the ordinary value of -1000 kPa in September to the exceptional value of 0 kPa in March, before dropping again to -1000 kPa in the following September. Similarly, the extraordinary dry season produces a linear decrease in the pore water pressure from the ordinary value of -100 kPa in March to the exceptional value of -2000 kPa in September, before increasing again to -100 kPa in the following March. These pore water pressure cycles are based on true field conditions, as recorded during long-term monitoring of slopes [8] but, for modelling purposes, they are schematised as simple linear trends between peak and troughs. Both perturbations occur after a sequence of several ordinary pore water pressure cycles at the ground surface which have caused the attainment of dynamic equilibrium conditions where each slope depth moves along the corresponding steady hysteretic loop.

After the perturbation, four ordinary pore water pressure cycles are imposed at the ground surface to evaluate the delay in regaining steady conditions. For the sake of brevity, simulations are only presented for two combinations of β_d and β_w, corresponding to case 3 and 4 in Table 3, while the parameters of the main curves are fixed at their respective base values in Table 1. Note that a

constant timestep $\Delta t = 1$ h has been adopted in the finite difference algorithm of Fig. 10.
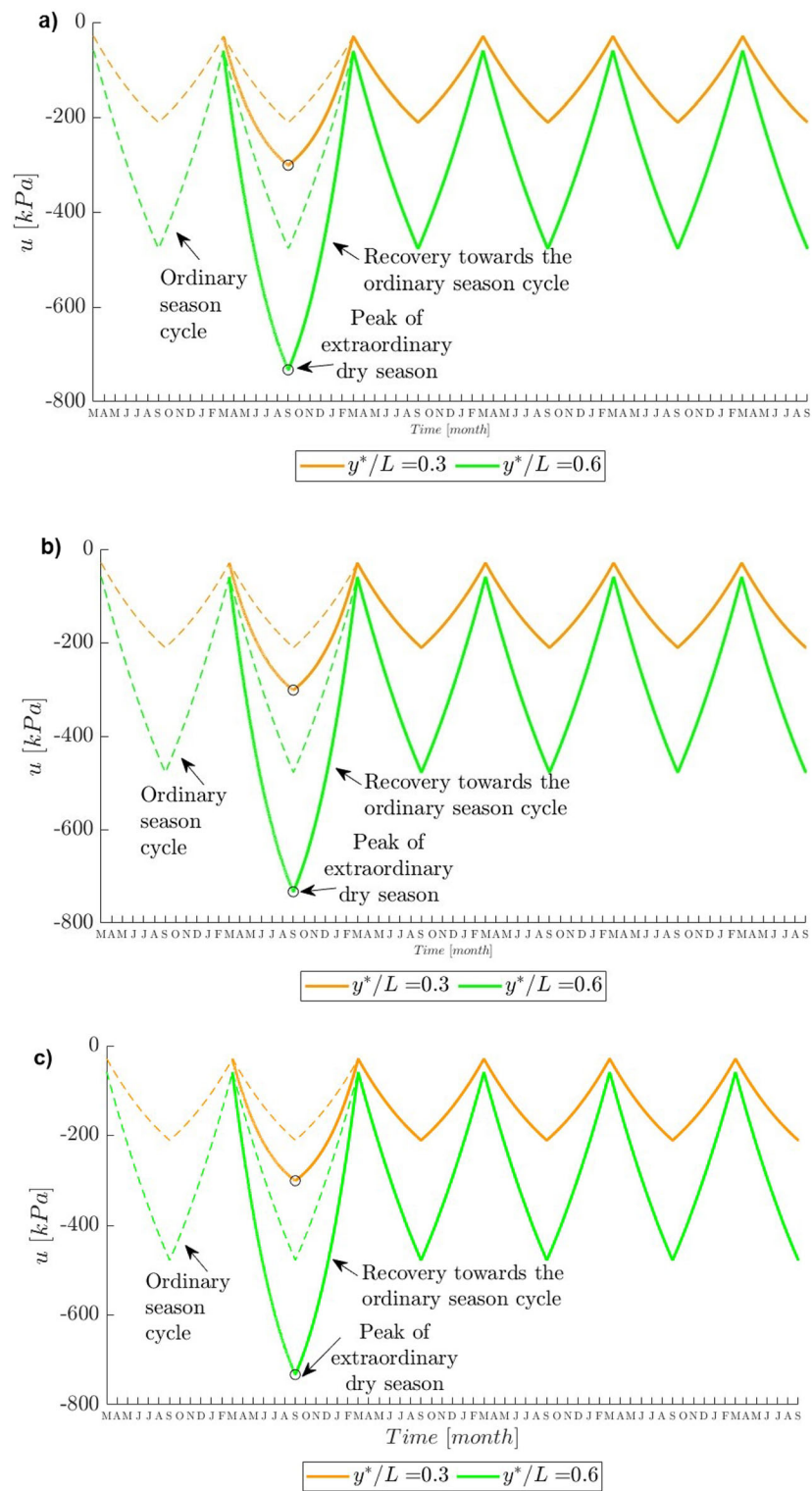
Figure 12 shows the effect of the extraordinary wet season on the evolution of degree of saturation at the two section coordinates $\frac{y^*}{L} = 0.6$ and $\frac{y^*}{L} = 0.3$, where the dashed and solid lines describe the ordinary and perturbed regimes, respectively. Figure 12a and b show the predictions of the two hysteretic models corresponding to cases 3 and 4, respectively, while Fig. 12c shows the prediction of the non-hysteretic model incorporating a reversible retention law given by Eq. (2) with parameter values equal to the average base values of the two main curves in Table 1.

Inspection of Fig. 12 indicates that the amplitude of the ordinary saturation cycle is larger for the non-hysteretic model than for the two hysteretic ones. This amplitude is also larger at the shallower depth (i.e. at $\frac{y^*}{L} = 0.6$) due to greater proximity to the surface where the cyclic boundary condition is applied. During the extraordinary wet season, the degree of saturation increases above the ordinary cycle by a significant amount for both hysteretic models while the increment is barely visible for the non-hysteretic model. Most importantly, after the perturbation, the two hysteretic models exhibit a slow descent towards ordinary conditions lasting several years, while the non-hysteretic model quickly regains the steady cycle after only one year. This is because, in the hysteretic case, each ground depth moves back gradually, year after year, towards the corresponding steady hysteretic loop as discussed in Sect. 3. Conversely, in the non-hysteretic case, the recovery of the steady retention path is virtually immediate after the ordinary suction cycle is reinstated. Inspection of Fig. 12a and b indicates that, in the hysteretic models, the number of years required to regain steady conditions increases with depth and strongly depends on the values of parameters β_d and β_w. When β_d and β_w are smallest as in case 3, a period between three and four ordinary years is enough to regain steady conditions (Fig. 12a) whereas, when β_d and β_w are largest as in case 4, a similar period of time is insufficient (Fig. 12b). The hysteretic models also exhibit some inertia in responding to the changing boundary condition at the ground surface as demonstrated by the increase in degree of saturation for some time after the perturbation is past its peak. This means that, at any given time, the retention trend may not be unique along the slope section and different depths may simultaneously move along a drying or wetting path.

Despite increased complexity, the hysteretic algorithm is very efficient, and the corresponding solution requires only a negligible increase in computational effort compared to the non-hysteretic one.

Figure 13 shows instead the effect of the extraordinary dry season on the evolution of degree of saturation as

Fig. 14 Effect of the extraordinary dry season on the evolution of pore water pressure at the two section coordinates $y^*/L = 0.3$ and $y^*/L = 0.6$: **a** hysteretic model of case 3, **b** hysteretic model of case 4 and **c** non-hysteretic model

predicted by the same models at the two section coordinates $\frac{y^*}{L} = 0.6$ and $\frac{y^*}{L} = 0.3$. The dashed lines of the ordinary cycles are identical to those of Fig. 12 and any visual

difference is simply due to the dissimilar scale of the vertical axis. The two hysteretic models predict a drop in degree of saturation that is slightly smaller than the

increase predicted during the extraordinary wet season. Instead, the non-hysteretic model predicts a decrease of degree of saturation that is markedly bigger than the increase predicted during the extraordinary wet season. Aside from these differences, the predictions of Fig. 13 are qualitatively similar to those of Fig. 12 and similar observations can be made about the evolution of degree of saturation over time. In particular, if the hysteretic nature of the soil is considered, several years of ordinary climate are required to erase the memory of the extraordinary dry season.

Finally, Fig. 14 shows the predicted pore water pressures at the two slope section coordinates $\frac{y^*}{L} = 0.6$ and $\frac{y^*}{L} = 0.3$ for the case of an extraordinary dry season. The predictions for the case of an extraordinary wet season are not presented in the sake of brevity, but they are qualitatively similar. Interestingly, Fig. 14 indicates that all three models calculate virtually identical pore water pressure cycles. This is in contrast with the predicted cycles of degree of saturation in Fig. 13, which are not only very different between hysteretic and non-hysteretic models, but also strongly dependant on the parameters of the hysteretic model. In particular, Fig. 14 shows that both hysteretic models regain the ordinary pore water pressure cycle immediately after the end of the perturbation whereas Fig. 13 shows a considerable time lag for the degree of saturation. This means that, at each ground depth, the post-perturbation recovery paths resemble those of Fig. 8, where the degree of saturation gradually grows towards the steady hysteretic loop while the pore water pressure is cycled over a virtually constant interval. The relatively little sensitivity of the pore water pressure cycles to the imposed perturbation may be a consequence of the chosen form of the relative permeability function which depends only on pore water pressure according to Eq. (10). To explore the sensitivity of the slope behaviour to the chosen conductivity model, future studies will introduce a dependency of the relative permeability function on degree of saturation.

6 Conclusions

This paper has presented a study of the long-term effects of an extraordinary climatic season on the hysteretic seepage across an infinite unsaturated soil slope, which has been modelled as a problem of one-dimensional infiltration normal to the slope by using the decomposition method of Bianchi et al. [5]. The hysteretic soil water retention law of Gallipoli et al. [21] has been implemented into the model and the resulting one-dimensional Richards' equation has been solved via a finite difference discretisation of the

slope cross section. A preliminary sensitivity analysis of the chosen retention law has allowed the selection of a realistic set of parameter values enabling a meaningful exploration of the effects of hydraulic hysteresis on the seepage regime.

The prolonged application of a stationary seasonal pore water pressure cycle at the ground surface generates a steady fluctuation of degree of saturation and pore water pressure inside the slope (i.e. the ordinary cycle), whose amplitude reduces as depth increases due to attenuated effect of the imposed boundary condition. In the case of degree of saturation, the amplitude of these fluctuations is also markedly different between hysteretic and non-hysteretic models.

The ordinary cycle has then been perturbed by an extremely wet or dry season, which produces a deviation of the seepage regime from steady conditions. In the hysteretic case, the steady cycle of degree of saturation is recovered after several years of ordinary climate whereas less than one year is needed in the non-hysteretic case. Therefore, if the hysteretic nature of the soil is considered, the "memory" of an extraordinary wet or dry season will only fade after a relatively long time of ordinary weather. Unlike degree of saturation, the steady cycle of pore water pressure is quickly regained after the perturbation, regardless of whether a hysteretic or non-hysteretic retention law is considered.

Finally, to increase confidence in the proposed modelling approach, the validity of the above predictions should be assessed against simultaneous measurements of both soil suction and water content from long-term field monitoring campaigns. Unfortunately, however, currently published data include measurements of either soil suction or water content, which is evidently not enough to calibrate and validate the present model. To remedy this shortcoming, a long-term field programme is currently under way to collect water content data [10, 12] and should be next complemented by measurements of soil suction to create a suitable modelling benchmark. Future work will also explore the influence of different relative permeability functions on model predictions and the evolution of the factor of safety during hysteretic seepage in both infinite and finite slopes.

Appendix

Bianchi et al. [5] proposed a methodology to solve the two-dimensional transient and steady state seepage across an unsaturated infinite slope via one-dimensional infiltration models. The main aspects of this methodology are recalled in the following, while further details are available in [5, 6].

Figure 9a provides a schematic representation of an infinite homogeneous unsaturated slope of thickness L (measured normal to the surface) and inclination β with respect to the horizontal. A constant pore water pressure u^{b} is imposed at the bottom of the slope, while either a constant pore water pressure u^{t} or a constant infiltration rate, normal to the ground, q^{t} is applied at the top.

The unsaturated soil permeability K is defined as:

$$K = \kappa_{\mathrm{r}} K^{\mathrm{sat}} \tag{13}$$

where κ_{r} is the relative unsaturated permeability function while K^{sat} is the constant saturated permeability. The saturated permeability can be further expressed as a function of the intrinsic permeability κ, the water specific weight γ_{w} and the water dynamic viscosity μ as:

$$K^{\mathrm{sat}} = \frac{\kappa \gamma_{\mathrm{w}}}{\mu} \tag{14}$$

In Fig. 9a, the seepage field is separated into antisymmetric and symmetric parts by decomposing the water specific weight γ_{w} into the two projections parallel $\gamma_{\mathrm{w}x^*}$ and perpendicular $\gamma_{\mathrm{w}y^*}$ to the slope. These two seepage parts can be individually solved and subsequently combined to calculate the actual flow regime.

The antisymmetric part of seepage is governed by the component of the water specific weight parallel to the slope $\gamma_{\mathrm{w}x^*}$ (Fig. 9a). In this case, every section perpendicular to the ground is an axis of antisymmetry and, hence, the corresponding flow field is parallel to the slope while the pore water pressure u^{asym} is zero everywhere. This implies that the antisymmetric piezometric head h^{asym} is calculated as:

$$h^{\mathrm{asym}} = -x^* + \frac{u^{\mathrm{asym}}}{\gamma_{\mathrm{w}x^*}} = -x^* \tag{15}$$

where the minus sign is introduced because the water specific weight component $\gamma_{\mathrm{w}x^*}$ and the x^* axis have the same direction.

The antisymmetric permeability K^{asym} is evaluated from Eq. (13) by introducing the component of the water specific weight parallel to the slope $\gamma_{\mathrm{w}x^*}$:

$$K^{\mathrm{asym}} = \kappa_r \frac{\kappa \gamma_{\mathrm{w}x^*}}{\mu} = \kappa_r \frac{\kappa \gamma_{\mathrm{w}}}{\mu} \sin \beta = K \sin \beta \tag{16}$$

Based on Eqs. (15) and (16) and Darcy's law, the two flux components $q_{x^*}^{\mathrm{asym}}$ and $q_{y^*}^{\mathrm{asym}}$ are then calculated as:

$$q_{x^*}^{\mathrm{asym}} = -K^{\mathrm{asym}} \frac{\partial h^{\mathrm{asym}}}{\partial x^*} = -K \sin \beta \frac{\partial h^{\mathrm{asym}}}{\partial x^*} = K \sin \beta \tag{17}$$

$$q_{y^*}^{asym} = -K^{asym} \frac{\partial h^{asym}}{\partial y^*} = -K \sin \beta \frac{\partial h^{asym}}{\partial y^*} = 0 \tag{18}$$

The symmetric part of seepage is governed by the component of water specific weight normal to the slope

$\gamma_{\mathrm{w}y^*}$ (Fig. 9a). In this case, every section perpendicular to the ground constitutes an axis of symmetry and the flow field is therefore perpendicular to the ground while the pore water pressure u^{sym} depends only on the y^* coordinate. This implies that the symmetric piezometric head h^{sym} is calculated as:

$$h^{\mathrm{sym}} = y^* + \frac{u^{\mathrm{sym}}}{\gamma_{\mathrm{w}y^*}} = y^* + \frac{u^{\mathrm{sym}}}{\gamma_{\mathrm{w}} \cos \beta} \tag{19}$$

The symmetric permeability K^{sym} is evaluated from Eq. (13) by introducing the component of the water specific weight perpendicular to the slope $\gamma_{\mathrm{w}y^*}$ in Eq. (14):

$$K^{\mathrm{sym}} = \kappa_{\mathrm{r}} \frac{\kappa \gamma_{\mathrm{w}y^*}}{\mu} = \kappa_{\mathrm{r}} \frac{\kappa \gamma_{\mathrm{w}}}{\mu} \cos \beta = K \cos \beta \tag{20}$$

Based on Eqs. (19) and (20), the flux components $q_{x^*}^{\mathrm{sym}}$ and $q_{y^*}^{\mathrm{sym}}$ are calculated as:

$$q_{x^*}^{sym} = -K^{\mathrm{sym}} \frac{\partial h^{sym}}{\partial x^*} = -K \cos \beta \frac{\partial h^{sym}}{\partial x^*} = 0 \tag{21}$$

$$\begin{aligned} q_{y^*}^{sym} &= -K^{\mathrm{sym}} \frac{\partial h^{sym}}{\partial y^*} = -K \cos \beta \frac{\partial h^{sym}}{\partial y^*} \\ &= -K \cos \beta \left(1 + \frac{1}{\gamma_w \cos \beta} \frac{\partial u^{sym}}{\partial y^*} \right) \end{aligned} \tag{22}$$

Note that the flux component parallel to the slope q_{x^*} coincides with the antisymmetric part $q_{x^*}^{\mathrm{asym}}$ of Eq. (17) because the symmetric part $q_{x^*}^{sym}$ is zero everywhere (Eq. 21):

$$q_{x^*} = q_{x^*}^{\mathrm{asym}} = K \sin \beta \tag{23}$$

Similarly, the flux component perpendicular to the slope q_{y^*} coincides with the symmetric part $q_{y^*}^{\mathrm{sym}}$ (Eq. 22) because the antisymmetric part $q_{y^*}^{\mathrm{asym}}$ (Eq. 18) is zero everywhere:

$$q_{y^*} = q_{y^*}^{\mathrm{sym}} = -K \cos \beta \left(1 + \frac{1}{\gamma_{\mathrm{w}} \cos \beta} \frac{\partial u^{\mathrm{sym}}}{\partial y^*} \right) \tag{24}$$

By comparing Eqs. (23) and (24) with the flux components, q_{x^*} and q_{y^*} calculated according to Darcy's law, the components of the gradient of the piezometric head h in the direction parallel and perpendicular to the slope are obtained as:

$$\frac{\partial h}{\partial x^*} = -\sin \beta \tag{25}$$

$$\frac{\partial h}{\partial y^*} = \cos \beta \left(1 + \frac{1}{\gamma_{\mathrm{w}} \cos \beta} \frac{\partial u^{\mathrm{sym}}}{\partial y^*} \right) \tag{26}$$

which can be integrated to obtain the actual piezometric head h as:

$$h = -x^* \sin \beta + y^* \cos \beta + \frac{u^{sym}}{\gamma_w} \tag{27}$$

Given the expression of the vertical coordinate $y = -x^* \sin\beta + y^* \cos\beta$, Eq. (27) implies that the pore water pressure field coincides with the symmetric one, i.e. $u = u^{\text{sym}}$. The two-dimensional seepage across an infinite slope can therefore be treated as the problem of one-dimensional infiltration perpendicular to a ground layer with permeability and water specific weight equal to $K\cos\beta$ and $\gamma_w\cos\beta$, respectively.

Author contributions All authors contributed to the study conception and design. Material preparation, data collection and analysis were performed by Bianchi Diana and Domenico Gallipoli. The first draft of the manuscript was written by Diana Bianchi and all authors commented on previous versions of the manuscript. All authors read and approved the final manuscript.

Data availability All data generated or analysed during this study are included in this published article.

Declarations

Conflict of interest The authors have no relevant financial or nonfinancial interests to disclose.

References

1. Albadri WM, Noor MJM, Alhani IJ (2021) The relationship between the shear strength and water retention curve of unsaturated sand at different hydraulic phases. Acta Geotech 16:2821–2835. https://doi.org/10.1007/s11440-021-01189-7

2. Azizi A, Jommi C, Musso G (2017) A water retention model accounting for the hysteresis induced by hydraulic and mechanical wetting-drying cycles. Comput Geotech 87:86–98. https://doi.org/10.1016/J.COMPGEO.2017.02.003

3. Bashir R, Sharma J, Stefaniak H (2016) Effect of hysteresis of soil-water characteristic curves on infiltration under different climatic conditions. Can Geotech J 53:273–284. https://doi.org/10.1139/cgj-2015-0004

4. Beber R, Tarantino A, Becker P (2023) Climate change adaptation of Elbe river flood embankments via suction-based design. Int J Geomech. https://doi.org/10.1061/IJGNAI.GMENG-7693

5. Bianchi D, Gallipoli D, Bovolenta R, Leoni M (2022) Analysis of unsaturated seepage in infinite slopes by means of horizontal ground infiltration models. Géotechnique. https://doi.org/10.1680/jgeot.22.00042

6. Bianchi D, Gallipoli D, Leoni M, Bovolenta R (2023) A methodology for modelling the flow regime in unsaturated infinite slopes. In: Proceedings 10th European conference on numerical methods in geotechnical engineering. https://doi.org/10.53243/NUMGE2023-305.

7. Bonan G (2019) Soil moisture. Climate change and terrestrial ecosystem modeling. Cambridge University Press, Cambridge, p 115

8. Bordoni M, Bittelli M, Valentino R, Chersich S, Meisina C (2017) Improving the estimation of complete field soil water characteristic curves through field monitoring data. J Hydrol (Amst) 552:283–305. https://doi.org/10.1016/j.jhydrol.2017.07.004

9. Borja RI, Liu X, White JA (2012) Multiphysics hillslope processes triggering landslides. Acta Geotech 7:261–269. https://doi.org/10.1007/s11440-012-0175-6

10. Bovolenta R, Iacopino A, Passalacqua R, Federici B (2020) Field measurements of soil water content at shallow depths for landslide monitoring. Geosciences 10(10):409. https://doi.org/10.3390/geosciences10100409

11. Bruno AW, Gallipoli D (2019) A coupled hydromechanical bounding surface model predicting the hysteretic behaviour of unsaturated soils. Comput Geotech 110:287–295. https://doi.org/10.1016/j.compgeo.2019.02.025

12. Campora M, Palla A, Gnecco I, Bovolenta R, Passalacqua R (2020) The laboratory calibration of a soil moisture capacitance probe in sandy soils. Soil Water Res 15(2):75–84. https://doi.org/10.17221/227/2018-SWR

13. Celia MA, Bouloutas ET, Zarba RL (1990) A general mass-conservative numerical solution for the unsaturated flow equation. Water Resour Res 26:1483–1496. https://doi.org/10.1029/WR026i007p01483

14. Chen J-M, Tan Y-C (2005) Analytical solutions of infiltration process under ponding irrigation. Hydrol Process 19:3593–3602. https://doi.org/10.1002/hyp.5847

15. Comegna L, Damiano E, Greco R, Olivares L, Picarelli L (2021) The hysteretic response of a shallow pyroclastic deposit. Earth Syst Sci Data 13:2541–2553. https://doi.org/10.5194/essd-13-2541-2021

16. Comegna L, Rianna G, Lee SG, Picarelli L (2016) Influence of the wetting path on the mechanical response of shallow unsaturated sloping covers. Comput Geotech 73:164–169. https://doi.org/10.1016/J.COMPGEO.2015.11.026

17. Egidi N, Gioia E, Maponi P, Spadoni L (2018) A numerical solution of Richards equation: a simple method adaptable in parallel computing. Int J Comput Math 97:2–17. https://doi.org/10.1080/00207160.2018.1444160

18. Farthing MW, Ogden FL (2017) Numerical solution of Richards' equation: a review of advances and challenges. Soil Sci Soc Am J 81:1257–1269. https://doi.org/10.2136/sssaj2017.02.0058

19. Fusco F, Bordoni M, Tufano R, Vivaldi V, Meisina C, Valentino R, Bittelli M, De Vita P (2022) Hydrological regimes in different slope environments and implications on rainfall thresholds triggering shallow landslides. Nat Hazards 114:907–939. https://doi.org/10.1007/s11069-022-05417-5

20. Gallipoli D (2012) A hysteretic soil-water retention model accounting for cyclic variations of suction and void ratio. Geotechnique 62:605–616. https://doi.org/10.1680/geot.11.P.007

21. Gallipoli D, Bruno AW, D'Onza F, Mancuso C (2015) A bounding surface hysteretic water retention model for deformable soils. Géotechnique 65:793–804. https://doi.org/10.1680/jgeot.14.P.118 (https://doi.org/10.1680/jgeot.2019.69.1.93)

22. Gallipoli D, Wheeler SJ, Karstunen M (2003) Modelling the variation of degree of saturation in a deformable unsaturated soil. Géotechnique 53:105–112. https://doi.org/10.1680/geot.2003.53.1.105

23. Gardner WR (1958) Some steady-state solutions of the unsaturated moisture flow equation with application to evaporation from a water table. Soil Sci 85:228–232. https://doi.org/10.1097/00010694-195804000-00006

24. Hu R, Hong JM, Chen YF, Zhou CB (2018) Hydraulic hysteresis effects on the coupled flow–deformation processes in unsaturated soils: numerical formulation and slope stability analysis. Appl Math Model 54:221–245. https://doi.org/10.1016/j.apm.2017.09.023

25. Huang RQ, Wu LZ (2012) Analytical solutions to 1-D horizontal and vertical water infiltration in saturated/unsaturated soils considering time-varying rainfall. Comput Geotech 39:66–72. https://doi.org/10.1016/j.compgeo.2011.08.008

26. Kool JB, Parker JC (1987) Development and evaluation of closed-form expressions for hysteretic soil hydraulic properties. Water Resour Res 23(1):105–114. https://doi.org/10.1029/WR023I001P00105

27. Ku C-Y, Liu C-Y, Su Y, Xiao J-E (2018) Modeling of Transient Flow in Unsaturated Geomaterials for Rainfall-Induced Landslides Using a Novel Spacetime Collocation Method. Geofluids 2018:1–16. https://doi.org/10.1155/2018/7892789

28. Kuo YL, Scott B, Jaksa M, Tidswell J, Treloar G, Treacy T, Richards P (2018) Numerical Modeling of Piled Retaining Wall in Unsaturated Adelaide Clays. In: Conference: 7th international conference on unsaturated soils (UNSAT 2018)

29. Langtangen HP, Linge S (2017) Finite difference computing with PDEs. Springer International Publishing, Cham

30. Likos WJ, Asce M, Lu N, Asce F, Godt JW (2014) Hysteresis and uncertainty in soil water-retention curve parameters. J Geotechn Geoenviron Eng 140:04013050. https://doi.org/10.1061/(ASCE)GT.1943-5606.0001071

31. Ma KC, Tan YC, Chen CH (2011) The influence of water retention curve hysteresis on the stability of unsaturated soil slopes. Hydrol Process 25:3563–3574. https://doi.org/10.1002/hyp.8081

32. Miao F, Wu Y, Li L, Tang H, Xiong F (2020) Weakening laws of slip zone soils during wetting–drying cycles based on fractal theory: a case study in the three Gorges reservoir (China). Acta Geotech 15:1909–1923. https://doi.org/10.1007/s11440-019-00894-8

33. Nguyen TS, Likitlersuang S (2019) Reliability analysis of unsaturated soil slope stability under infiltration considering hydraulic and shear strength parameters. Bull Eng Geol Env 78:5727–5743. https://doi.org/10.1007/s10064-019-01513-2

34. Nian G, Chen Z, Zhang L, Bao M, Zhou Z (2023) Three-dimensional stability analysis of unsaturated slopes under variable rainfall conditions using a numerical method. Bull Eng Geol Env 82:59. https://doi.org/10.1007/s10064-023-03082-x

35. Paniconi C, Putti M (1994) A comparison of Picard and Newton iteration in the numerical solution of multidimensional variably saturated flow problems. Water Resour Res 30:3357–3374. https://doi.org/10.1029/94WR02046

36. Parker JC, Lenhard RJ (1987) A model for hysteretic constitutive relations governing multiphase flow 1. Saturation-pressure relations. Water Resour Res 23(12):2187–2196

37. Richards LA (1931) Capillary conduction of liquids through porous mediums. Physics 1:318–333. https://doi.org/10.1063/1.1745010

38. Rouainia M, Helm P, Davies O, Glendinning S (2020) Deterioration of an infrastructure cutting subjected to climate change. Acta Geotech 15:2997–3016. https://doi.org/10.1007/s11440-020-00965-1

39. Šimůnek by J, Šejna M, Saito H, Sakai M, Th van Genuchten M (2013) The HYDRUS-1D software package for simulating the one-dimensional movement of water, heat, and multiple solutes in variably-saturated media

40. Stoffel M, Tiranti D, Huggel C (2014) Climate change impacts on mass movements—case studies from the European Alps. Sci Total Environ 493:1255–1266. https://doi.org/10.1016/j.scitotenv.2014.02.102

41. Tan Y-C, Ma K-C, Chen C-H, Ke K-Y, Wang M-T (2009) A numerical model of infiltration processes for hysteretic flow coupled with mass conservation. Irrig Drain 58:366–380. https://doi.org/10.1002/ird.403

42. Wang J, Zhang D, Zhang Y, Chen H, Ma W (2022) Variations in hydraulic properties of collapsible loess exposed to wetting and shearing. Acta Geotech 17:2995–3015. https://doi.org/10.1007/s11440-021-01427-y

43. Wu LZ, Huang RQ, Xu Q (2012) Incorporating hysteresis in one-dimensional seepage modeling in unsaturated soils. KSCE J Civ Eng 16:69–77. https://doi.org/10.1007/s12205-012-1377-z

44. Yang C, Sheng D, Carter JP (2012) Effect of hydraulic hysteresis on seepage analysis for unsaturated soils. Comput Geotech 41:36–56. https://doi.org/10.1016/j.compgeo.2011.11.006

45. Yang C, Sheng DC, Carter JP (2011) Numerical modelling of hydraulic hysteresis in unsaturated soil covers. In: 13th international conference of the international association for computer methods and advances in geomechanics (IACMAG2011). Computer methods for geomechanics: frontiers and new applications. Melbourne. pp 741–746

46. Zhan TLT, Jia GW, Chen Y-M, Fredlund DG, Li H (2013) An analytical solution for rainfall infiltration into an unsaturated infinite slope and its application to slope stability analysis. Int J Numer Anal Methods Geomech 37:1737–1760. https://doi.org/10.1002/nag.2106